WARSAW UNIVERSITY OF TECHNOLOGY Index 351733
FACULTY OF CIVIL ENGINEERING
COMMITTEE FOR CIVIL AND WATER ENGINEERING
POLISH ACADEMY OF SCIENCES ISSN 1230-2945

DOI: 10.24425/ace.2026.1417

ARCHIVES OF CIVIL ENGINEERING

Vol. LXXII ISSUE 3 2026

pp. 585 –602

Research paper

Strength characteristics and failure mechanism of rock-like specimen with cracks under biaxial cyclic compression

Tao Wu[1], Xiaoqiang Xue[2], Chenpu Li[3]

Abstract: In order to study the strength characteristics and failure mechanism of fissured rocks under biaxial cyclic compression, taking Zheduoshan metamorphic sandstone as the reference object, orthogonal design of sandstone like sample mix proportion was carried out based on the principle of similarity, and samples with different dip angles and crack lengths were prepared. Based on theoretical analysis, indoor tests and PFC^{2D} numerical simulations were conducted to study the strength characteristics and failure mechanism of rock-like materials with crack under biaxial conventional loading and biaxial cyclic loading and unloading conditions. The results show that cracks are an important factor affecting the strength of rock masses. As the length of cracks increases and the inclination angle of cracks approaches 45°, the peak stress of the sample will gradually decrease. The peak stress of the sample under cyclic loading and unloading conditions is smaller than that under conventional loading, and lateral pressure can also improve the peak strength of the sample under external loading. The connection modes of fractured rocks under biaxial loading can be divided into three types: tensile connection, shear connection, and tensile-shear composite connection, and the penetration modes are affected by the inclination angle of the fissure, with tensile penetration mainly occurring at inclination angles of 0°–30°, tensile-shear composite penetration occurring at angles of 45°–60°, and shear penetration mainly occurring at 90°.

Keywords: artifical rock specimen, biaxial compression test, failure mechanism, fissured rock, PFC^{2D}

[1]M.Eng., College of Environment and Civil Engineering, Chengdu University of Technology, Chengdu 610059, China, e-mail: 747351297@qq.com, ORCID: 0009-0008-8746-791X
[2]A.P., PhD., Eng., College of Environment and Civil Engineering, Chengdu University of Technology, Chengdu 610059, China, e-mail: xuexiaoqiang@cdut.cn, ORCID: 0009-0000-2703-7338
[3]M.Eng., College of Environment and Civil Engineering, Chengdu University of Technology, Chengdu 610059, China, e-mail: lichenpu@stu.cdut.edu.cn, ORCID: 0009-0005-4713-9186

1. Introduction

The rock body in nature will produce joints, fissures, soft rock strata and other structural plane under long-term tectonic stress, and the fissured rock body is the heterogeneous and discontinuous composite structural body composed of rock mass and structural plane. Its strength characteristis and fissure expansion and destruction mechanism are not only controlled by the rock mass, but also mainly influenced by the characteristics of fissure development and rock structure in the rock body.

The effect of fracture geometry on the strength characteristis of rocks has been investigated by a number of researchers by carrying out a large number of uniaxial and multiaxial compression tests. It was found that the strength of fissured rocks depends on the inclination angle of the cracks as well as the length of the cracks. The peak strength of fissured rock decreases with increasing crack length, decreasing and then increasing with increasing crack inclination, with a minimum at 45° [1–7]. When the crack inclination angle is small, the peak strength of the specimen decreases with the increase of crack density; when the inclination angle is large, the crack density has no significant effect on the peak strength of the specimen; and at the same crack density, the peak strength of the specimen shows an increasing trend with the increase of crack inclination angle [8]. At a certain crack angle, the initial deformation of the specimen decreases with the increase of the non-overlapping length of the crack, the peak strength decreases and then increases, and the peak strain increases and then decreases [9]. In addition to this, the confining pressure has a certain degree of influence on the strength of the fractured rock, Tang [10, 11] by determining the mechanical behavior, and failure modes of rectangular green sandstone specimens containing individual joints with different inclinations under different circumferential pressures, found that the circumferential pressure has an enhancing effect on the peak strength, residual strength, and the threshold of fracture damage of the green sandstone, and has a decreasing effect on the anisotropy of the jointed rock.

The macroscopic failure process of fractured rock was an evolution process of rock from the microscopic level to macroscopic level that resulted from the interaction of internal particles under compression loading. The distribution pattern of prefabricated fractures had a great influence on the failure mode and plays an important role in the macroscopic characteristics and the evolution of internal components of pre-fractured rock specimens [12]. It was found that in uniaxial and biaxial compression tests, as the axial load increases, new cracks emerged from preformed flaws and eventually coalesced [13]. The newly created cracks are wing cracks caused by tensile stresses and anti-wing cracks initiated by compressive shear stresses, respectively. Both types of cracks start at the pre-crack tip, and the larger the pre-crack angle, the larger the initial crack angle [14]. The location of stress concentration and crack initiation varies with the location of the pre-cracking angle, and the crack distribution shows a "V" trend, with tensile cracks dominating and some shear cracks [7].

Meanwhile, in order to better verify the reliability of the test results, there are many researchers using different numerical simulation methods for comparative verification. Most of them are based on PFC^{2D} and use different cell methods to simulate the cracking process of fractured rocks [15–18], some scholars proposed a coupling study between loading and unloading and seepage stresses [18]. Some researchers have also used PFC3D (Particle Flow Code in 3 Dimensions) and GPD3D (General particle dynamics in 3 Dimensions) to study the failure process of fissure-type rock materials from a three-dimensional perspective [19–21].

With the development of numerical simulation software technology, in recent years, some researchers have used discrete element-based method to build models and extended finite element method combined with cohesion model for numerical simulation [22, 23].

At present, the research on the strength characteristics and destrucion mechanism of fractured rock masses mainly focuses on the conventional uniaxial test and triaxial tests. There is still little research on biaxial conventional loading and biaxial cyclic loading and unloading tests of fractured rock masses. On this basis, there is almost no test research which considers factors such as crack length, crack inclination angle, lateral pressure, and number of cycles simultaneously. The corresponding theoretical models are also rarely proposed by scholars. Therefore, on the basic of theoretical analysis, this paper analyses the strength characteristics and failure mechanism of fractured rock masses under biaxial loading and unloading conditions by conducting indoor biaxial loading tests on rock-like materials with cracks and uses PFC^{2D} for numerical simulation to compare the results of the test and numerical simulation.

2. Methods and materials

2.1. Sample preparation

The specimen size of 100 × 100 × 100 mm cube, using standard 325 ordinary silicate cement, quartz sand (particle size 0.50–1.00 mm) and tap water in accordance with the ratio of 1:2:0.45 made into sandstone specimens. The prefabricated fissures in the specimen are made from PVC plastic sheets of specified size, and the prefabricated fissure-like sandstone specimen is shown in Fig. 1. In the figure, “α” denotes the fissure inclination (relative to the axial force loading direction), “L” denotes the fissure length, the direction indicated by “σ_1” is the axial force loading direction, and the direction indicated by “σ_3” is the lateral force loading direction.

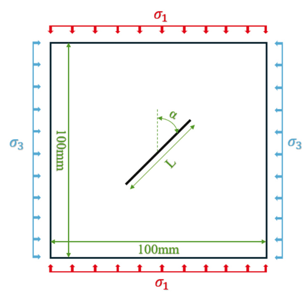

Fig. 1. Schematic diagram of prefabricated fractured rock samples

2.2. Test equipment

The test equipment adopts YDS-SF-3 microcomputer servo control rock mechanics test system, as shown in Fig. 2. Biaxial conventional loading and biaxial cyclic loading and unloading of the two loading methods and the lateral pressure will be taken as 2 MPa, 4 MPa. the specimen in addition to the prefabricated crack surface of the other two directions of the loading, the control mode of the use of stress control, the loading speed of 5 kN/s.

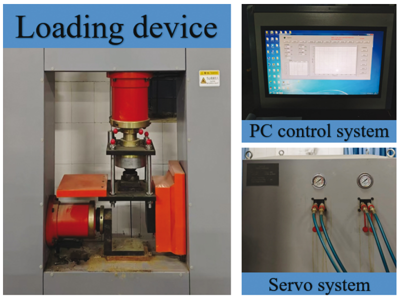

Fig. 2. The YDS-SF-3 rock mechanics test equipment

The plan considers the effects of crack length, crack inclination angle, lateral pressure, and number of cycles on the biaxial conventional loading and biaxial cyclic loading and unloading tests of fractured sandstone. Combined with existing test conditions, the specific settings for crack length, crack inclination angle, lateral pressure, and number of cycles are as follows:

(1) Crack lengths (L) for 20 mm, 40 mm, 60 mm, and 80 mm.

(2) Crack inclination angle (α) for 0°, 30°, 45°, 60°, and 90°.

(3) Lateral pressures of 2 MPa and 4 MPa.

(4) In the biaxial cyclic loading and unloading test, the number of cycles is 4.

3. Particle flow modelling

The conventional biaxial loading test was carried out on the intact specimen, and the same mathematical model as that of the test specimen was established based on the test data using PFC^{2D}. The particles were uniformly and randomly distributed with particle size sizes ranging from 0.3 mm to 0.5 mm. 17620 spheres were generated from the complete specimen, and the particles were constrained by 4 boundary walls, with a uniform distribution of particle size. For prefabricated fissures a wall with the geometry of the desired fissure is generated in the centre of the full model, and then all remaining particles are rebalanced after all particles within the wall have been removed. After all particles are rebalanced the generated wall and the out-of-size granular body are deleted, and a granular model of the rock body with the desired fissure is obtained. Since the PFC cannot apply a force directly to the wall, the simulation is servoed by applying a certain velocity to the wall, with a displacement rate of 0.05 mm/s.

For the contact model between particles, a parallel bonding model is used for bonding. The parallel bonding model incorporates a bonding surface consisting of a cementitious material with a certain thickness in the contact portion of the particles, which can be regarded as a disc with a certain thickness in PFC^{2D}, capable of transmitting forces and moments, and the strength of the bond depends on the maximum normal and tangential stresses, and when the normal and tangential stresses are greater than their corresponding strengths the bond is broken, and the forces, moments, and stiffnesses will be removed by the procedure. This model is defined by the parameters of normal stiffness $\overline{K}^n$, tangential stiffness $\overline{K}^s$, normal bond strength $\overline{\sigma}_c$ tangential bond strength $\overline{\tau}_c$, and the connection radius $\overline{R}$, and the schematic diagram of the parallel bond model is shown in Fig. 3.

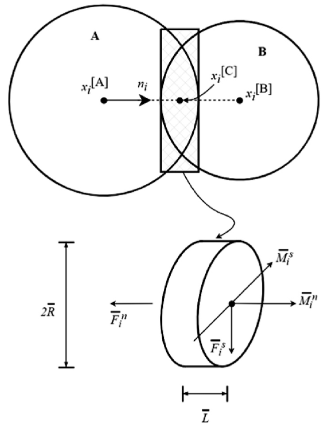

Fig. 3. Schematic diagram of parallel bonding model

The model total contact force and moment are $\overline{F}_i$ and $\overline{M}_i$, respectively, which can be decomposed into the sum of normal and tangential components as shown in Eq. (3.1).

$$\begin{cases} \overline{F}_i = \overline{F}_i^n + \overline{F}_i^s \\ \overline{M}_i = \overline{M}_i^n + \overline{M}_i^s \end{cases} \tag{3.1}$$

where, $\overline{F}_i^n$ and $\overline{F}_i^s$ are the normal and tangential components of the contact force, and $\overline{M}_i^n$ and $\overline{M}_i^s$ are the normal and tangential components of the moment, respectively. The initial values of $\overline{F}_i$ and $\overline{M}_i$ in the parallel bonding model are 0. After 1 step, the relative motion of the particles will generate displacement increments and rotation increments, and the contact force and moment will be updated, and the equations for the update of the normal and tangential components of the forces and moments in 1 step Δt are shown in Eq. (3.2).

$$\begin{cases} \Delta\overline{F}_i^n = \left(-\overline{K}^n A\Delta U^n\right) \boldsymbol{n}_i \\ \Delta\overline{F}_i^s = -\overline{K}^s A\Delta U_i^s \\ \Delta\overline{M}_i^n = -\left(\overline{K}^s J\Delta\theta^n\right) \boldsymbol{n}_i \\ \Delta\overline{M}_i^s = -\overline{K}^n I\Delta\theta_i^s \end{cases} \tag{3.2}$$

$$\begin{cases} \overline{F}_i^n \leftarrow \overline{F}_i^n \boldsymbol{n}_i + \Delta\overline{F}_i^n \\ \overline{F}_i^s \leftarrow \overline{F}_i^s + \Delta\overline{F}_i^s \\ \overline{M}_i^n \leftarrow \overline{M}_i^n \boldsymbol{n}_i + \Delta\overline{M}_i^n \\ \overline{M}_i^s \leftarrow \overline{M}_i^s + \Delta\overline{M}_i^s \end{cases} \tag{3.3}$$

where: ΔU^n and ΔU_i^s are normal and tangential displacement increments, respectively; A is the cross-sectional area; n_i is the unit normal vector at the contact; $\Delta\theta^n$ and $\Delta\theta_i^s$, are the normal and tangential angular displacement increments, respectively; I and J denote the polar moment of inertia of the parallel bonded section and the polar distance moment of inertia of the contact point, respectively. The iterative process of force and moment vectors is obtained by superposing the force and moment at the previous step with the increments of the updated force and moment at the next step, as shown in Eq. (3.3).

According to the theory of beam section, the parallel bond is subjected to maximum tensile and shear stresses calculated as shown in Eq. (3.4). When $\sigma_{\max}$ is greater than the normal bond strength $\overline{\sigma}_c$, the model belongs to tensile damage; when $\tau_{\max}$ is greater than the tangential bond strength $\overline{\tau}_c$, the model belongs to shear damage.

$$\begin{cases} \sigma_{\max} = \dfrac{-\overline{F}^n}{A} + \dfrac{|\overline{M}_i^s|\overline{R}}{I} \\ \tau_{\max} = \dfrac{|\overline{F}_i^s|}{A} + \dfrac{|\overline{M}^n|\overline{R}}{J} \end{cases} \tag{3.4}$$

The numerical simulation parameters used are shown in Table 1. By adjusting the values to obtain reasonable fine-view parameters, the numerical simulation results were finally made to be basically consistent with the indoor test results of the complete specimen, as shown in Fig. 4, it can be seen that the results of the numerical simulation are more ideal, which is due to the fact that the particles within the model are regenerated and compacted by the numerical simulation software, and the contact between the particles is relatively homogeneous, and thus the stress-strain curves of the numerical simulation model are almost straight lines throughout the whole period before peak value. Stage is almost straight line, all approximate to the elastic deformation.

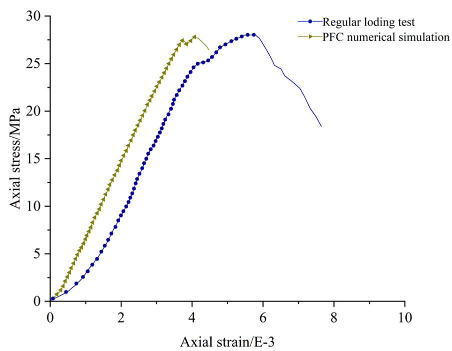

Fig. 4. Stress-strain curves of complete samples under 2 MPa lateral compression under biaxial conventional loading test and numerical simulation

Table 1. Particle micro parameter values

Coefficient of friction	Parallel bonding modulus (GPa)	Parallel bonding stiffness ratio	Adhesive tensile strength (MPa)	Adhesive force (MPa)	Parallel bonding friction angle (°)
0.5	8.0	1.5	13.5	13.5	34

4. The analysis of strength characteristics

4.1. Analysis of stress-strain curve

Through indoor tests, the axial stress-strain curves of the specimens under conventional biaxial loading and cyclic loading were obtained. During the research process, it was found that the peak stress of the complete specimen was the highest, indicating that the presence of cracks led to the formation of deterioration inside the specimen, resulting in a decrease in its peak stress. When the axial stress reaches the peak value, the rock rapidly fractures and produces a deafening sound, while rapidly generating a large number of macroscopic cracks.

The $\alpha = 60°$, $L = 40$ mm crack specimen is now studied as an example to analyse its axial stress-strain curves under conventional biaxial loading as well as cyclic loading tests at lateral pressure of 2 MPa, as shown in Fig. 5.

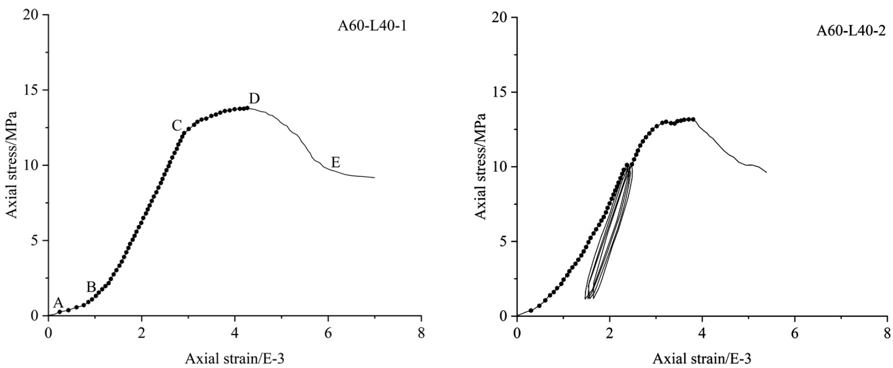

(a) (b)

Fig. 5. Axial stress-strain curve of $\alpha = 60°$, $L = 40$ mm fractured sample: (a) Regular loading, (b) Cyclic loading

Under biaxial conventional loading, the axial stress-strain curves of rock specimens containing prefabricated cracks show a slight concave shape during the initial loading stage (A-B section in Fig. 5a). At this time, the small cracks that initially existed inside the specimen are in a gradually compacted process. Continue to load, the slope of the curve remains roughly constant below a certain strain value, and after unloading the specimen at this stage, the axial strain can still have a certain degree of recovery, which means that it is in the elasticity stage to the stage of microcrack extension (B-C section in Fig. 5a). When the axial stress continues to increase, the curve begins to show an upward convex shape, and the slope of the curve begins to decrease, from the elastic characteristic to the plastic characteristic excessively, and enters the stage of rupture development (section C-D in Fig. 5a). When the axial stress grows to the compressive strength value of the specimen, the peak stress value, the specimen is rapidly destabilized and damaged, and the axial stress starts to fall and enters the post-peak stage (section D-E in Fig. 5a). It can be found that compared with the uniaxial loading, the post-peak curve of the biaxially loaded specimen shows a slower fall in the stress, due to the presence of the lateral pressure which restricts the lateral deformation of the specimen.

As can be seen through Fig. 5b, due to the intervention of cyclic loading and unloading, the axial stress-strain curve of the specimen shows an obvious cyclic loading and unloading characteristic - hysteresis loop. In the early stages of the loading and unloading cycle, the loading and unloading curves do not exactly coincide, and the path of the unloading curve is lower than the path of the loading curve. The paths of the loading and unloading curves in the same cycle form a blade shape, which is narrower at both ends and wider in the middle. As the number of cyclic loading and unloading increases, the hysteresis loops gradually become denser and their shapes more complete in the middle of cyclic loading and unloading. At the same time, it can be seen that the position of the hysteresis loop is gradually moving to the right, and the axial strain corresponding to the same axial stress on the curve increases. When the specimen is removed from the cyclic loading and unloading, the axial stress continues to rise and reaches a critical value, the irreversible deformation inside the fissure rock specimen gradually increases, resulting in the rupture of the specimen.

Then we take $\alpha = 0°$, $L = 40$ mm crack specimen in biaxial conventional loading test and simulation results comparison; $\alpha = 30°$, $L = 60$ mm crack specimen in biaxial cyclic loading test and simulation results comparison as an example for the study and analyse its axial stress-strain curve. As shown in Fig. 6.

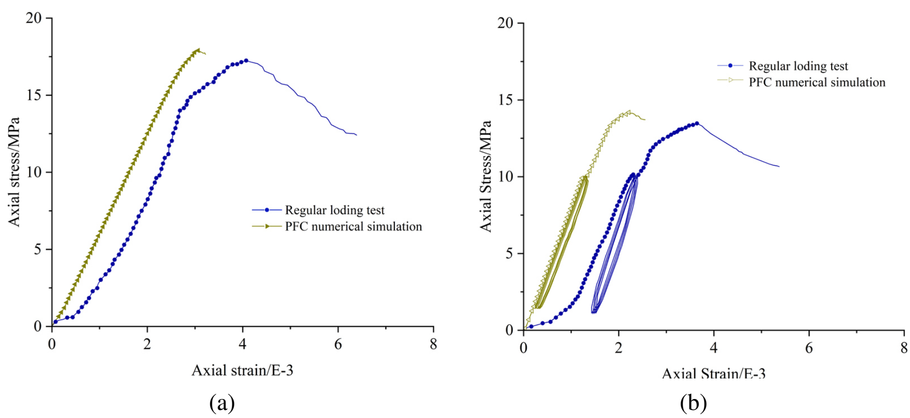

Fig. 6. (a) Stress-strain curves of $\alpha = 0°$, $L = 40$ mm samples under biaxial conventional loading test and numerical simulation (regular loading), (b) Stress-strain curves of $\alpha = 30°$, $L = 60$ mm samples under biaxial cyclic loading test and numerical simulation (cyclic loading)

As can be seen from Fig. 6, the stress-strain curves obtained from the biaxial conventional loading and biaxial cyclic loading indoor tests are relatively similar with the numerical simulation results, but the numerical simulation results are more idealized. This is due to the fact that the particles in the model are regenerated and compacted by the numerical simulation PFC^{2D} software during the initial modelling, and the contact between the particles is relatively homogeneous, so the stress-strain curves of the numerical simulation model are almost straight lines throughout the whole stage before the peak value, which are all approximate to the elastic deformation. And the effect of cyclic loading and unloading on the model stress-strain curve is very limited.

4.2. Impact of crack angle

The peak stresses of the rock-like specimens with crack under conventional biaxial loading as well as cyclic loading and unloading with a lateral pressure of 2 MPa and the numerically simulated peak stresses are counted as shown in Fig. 7.

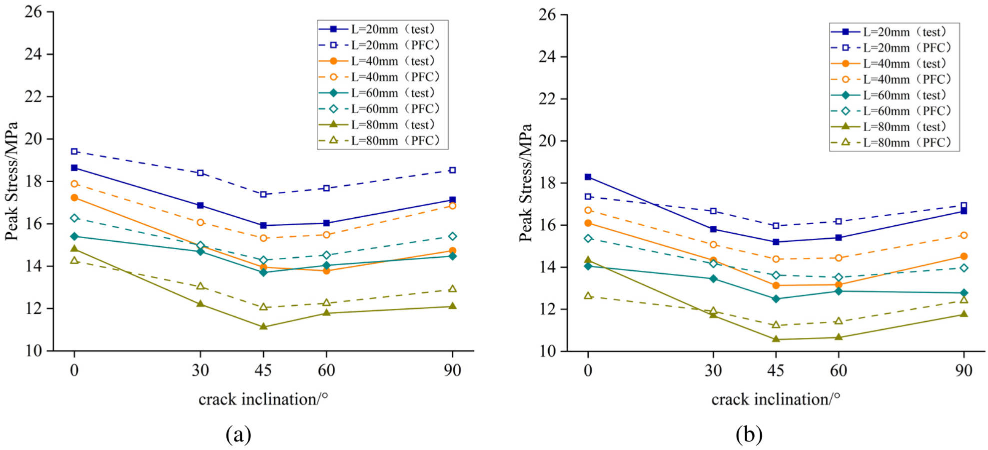

Fig. 7. Peak stress-crack inclination curve: (a) Regular loading, (b) Cyclic loading

Analysing the peak stress-crack inclination angle (α) relationship curve, it can be seen that the peak stress of the specimen is significantly affected by the crack angle. When the crack length (L) is the same, the α from 0° to expand to 45° in the process, the peak stress with the α increases and shows a decreasing trend, this rule of change in the 0°, 30°, 45° specimens are almost the same. When the α from 45° to 90°, the peak stress of the specimen has been rebounded (only in the $L = 40$ mm, α from 45° expand to 60°, the peak stress further decline), but the peak stress is still smaller than $\alpha = 0°$.

This law shows that whether under biaxial conventional loading or cyclic loading, the peak stress of the rock-like specimen with crack shows a more obvious "V" type relationship with the crack angle, the peak stress is lowest when $\alpha = 45°$ and narrowing down from 45° to 0° or enlarging from 45° to 90° will increase the peak stress of the specimen.

By comparing the peak stress-crack angle curves under the two loading methods, it was found that under the same lateral pressure conditions and specimen geometry, the peak stress of cyclic loading specimens was lower than conventionally loaded specimens.

The fitted curves of peak stress and crack angle under cyclic loading and unloading conditions are shown in Fig. 8. It can be seen that the fitted curves of the test data and the fitted exponential function equations all have a high degree of fit, and the values of strength coefficients of the curves e^a are more stable for the fitted curves of the specimen groups with different crack lengths, which indicates that there is an exponential relationship between the peak stresses and crack inclination angle of rock-like specimens with crack at the same crack length.

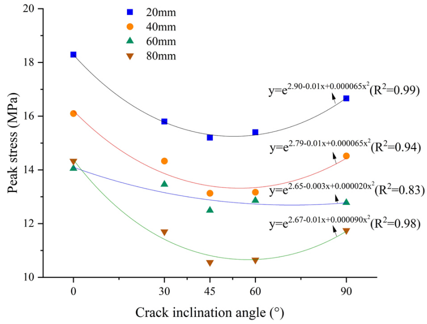

Fig. 8. Fitting curve of peak stress-crack inclination angle relationship

4.3. Impact of crack length

The peak stress-crack length (L) comparison was statistically analysed for the rock-like specimens with crack under conventional biaxial loading as well as cyclic loading and unloading at a lateral pressure of 2 MPa, grouped according to the same crack inclination angle, and the results are shown in Fig. 9.

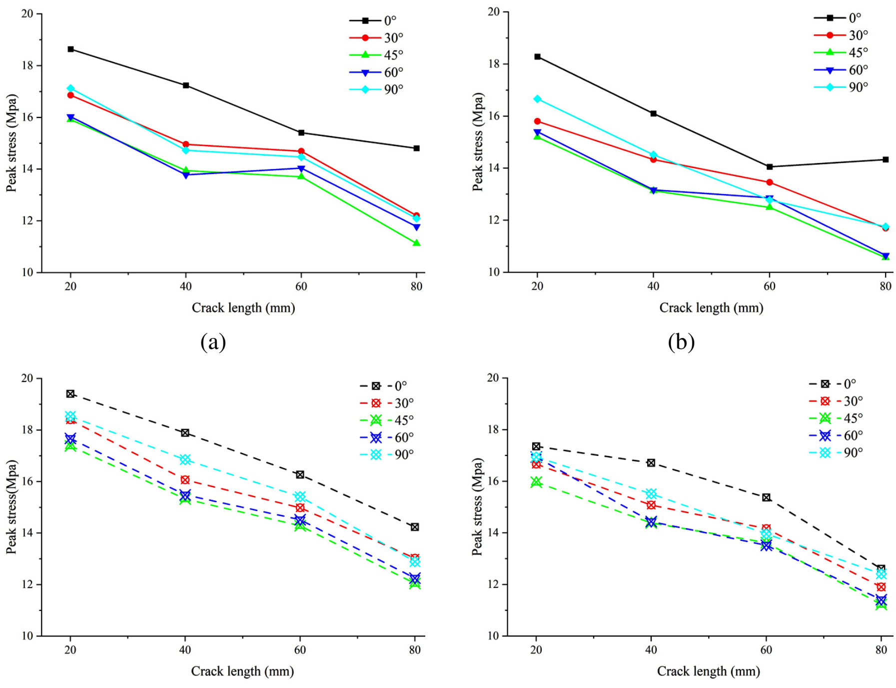

Fig. 9. Peak stress-crack length curve: (a) Regular loading test, (b) Cyclic loading test, (c) Numerical simulation of regular loading test, (d) Numerical simulation of cyclic loading test

When the crack inclination angle is the same, for the specimens at the same lateral pressure level, the peak stress of the specimen decreases with the increase of crack length (L) from 20 mm to 80 mm (in the conventional loading test, only when $\alpha = 0°$, L increases from 40 mm to 60 mm specimen; as well as cyclic loading and unloading test, only when $\alpha = 0°$, L increases from 60 mm to 80 mm peak stress has recovered, the rest of the specimens are satisfied this law). The decrease in peak stress of the specimen is greater when the crack length (L) expands from 20 mm to 40 mm or from 60 mm to 80 mm.

This indicates that the peak stress of rock-like specimens with crack deteriorates with increasing crack length under both loading conditions, and the larger the relative value of crack length, the higher the degree of deterioration. There is a significant negative correlation between the peak stress and the crack length of the rock-like specimens with crack.

The fitted curves of crack length and peak stress under cyclic loading and unloading conditions are shown in Fig. 10. It can be seen that the fitted curves of the test data fitted well with the fitted exponential function which indicates that there is a negative exponential relationship between the peak stress and crack length of rock-like specimens with crack under the same crack angle.

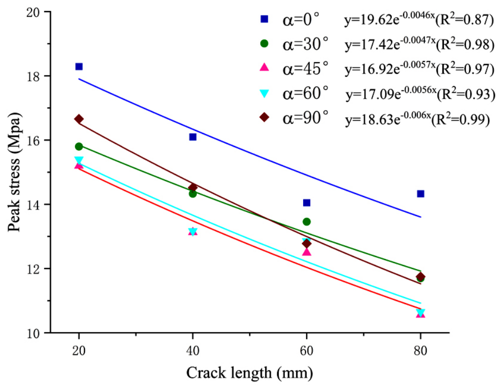

Fig. 10. Fitting curves of peak stress-crack length relationship

4.4. Impact of lateral pressure

To analyse the stress-strain curve of the same specimen under different lateral pressures, the conventional loading is shown in Fig. 11(a) for $\alpha = 90°$, $L = 40$ mm specimen, and the cyclic loading is shown in Fig. 11(b) for $\alpha = 30°$, $L = 60$ mm specimen.

From Figures 7 and 9, it can be found that the crack geometry has almost no effect on the overall shape of the stress-strain curve of the specimen at a certain lateral pressure. However, it can be seen from Fig. 11 that the peak stresses in the specimens with the same fracture geometry at lateral pressure of 4 MPa are greater than the peak stresses at lateral pressure of 2 MPa, both for conventional loading and cyclic loading. The increase in lateral pressure leads to an increase in the peak stress of the specimen and a decrease in the value of strain required for the specimen to reach the peak stress. When the lateral pressure increases from 2 MPa to

4 MPa, the overall inclination of the axial stress-strain curve of the specimen becomes larger, and the demarcation point between the pore-compacting stage and the elastic deformation stage becomes more obvious, and the up-concave portion of the curve is more short-lived; in addition, the plastic deformation interval of the specimen in the curve is also shortened.

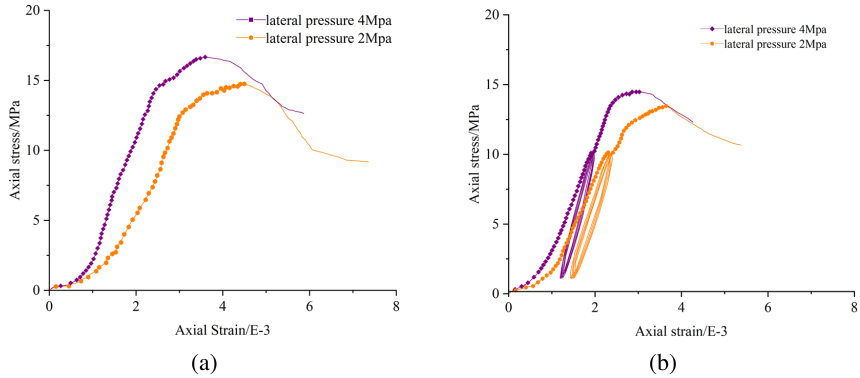

Fig. 11. (a) The stress-strain curves of $\alpha = 90°$, $L = 40$ mm samples under different lateral pressures (regular loading); (b) The stress- strain curves of $\alpha = 30°$, $L = 60$ mm samples under different lateral pressures (cyclic loading)

In order to investigate the effect of lateral pressure on the peak stress of conventionally loaded and cyclically loaded specimens, the peak stresses of specimens under two lateral pressure conditions of 2 MPa and 4 MPa were statistically compared and analysed as shown in Fig. 12.

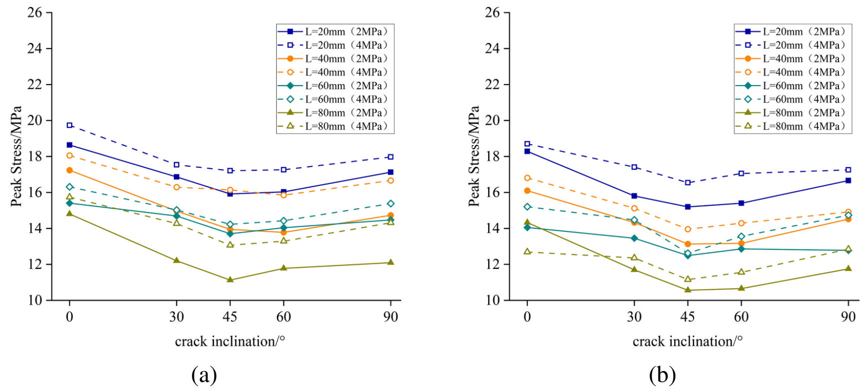

Fig. 12. Curves of peak stress of samples under different lateral pressures: (a) Regular loading, (b) Cyclic loading

According to Fig. 12, it can be seen that after the lateral pressure was increased from 2 MPa to 4 MPa, the specimen still showed a "V" type correspondence by the change of the crack inclination angle, and still showed a negative correlation by the change of the crack length, which indicated that the increase of the lateral pressure did not lead to a change of the trend of the influence of the crack geometry on the peak stress of the specimen.

Under the two loading conditions, the peak stress of the same crack specimen increases with the increase of lateral pressure when the crack length (L) and the crack inclination angle (α) are the same. This indicates that the increase in lateral pressure has a certain strengthening effect on the peak stress of the specimen. It can be predicted that when the value of lateral pressure increases to a sufficient degree, the peak strength of the crack-containing specimen will infinitely converge to that of the intact specimen, which is mainly due to the existence of the lateral pressure that makes the specimen partially closed inside the micropore, which to a certain extent restricts the lateral displacement that occurs during the failure of the specimen, and thus improves the compressive strength of the specimen.

5. The analysis of failure mechanism

Two types of cracks, wing cracks and secondary cracks, were found at the end of the crack. Wing cracks usually appear at the crack end at an angle (wing cracks that form an acute angle with the direction of crack extension are called anti-wing cracks) and are stable towards the direction of the maximum principal stress; secondary cracks are shear cracks, which also appear at the crack end, but the difference is that the secondary cracks are relatively stable at the time of their appearance, and then they may develop towards instability. The classification of crack penetration patterns in this test is shown in Table 2.

Table 2. Classification of crack penetration patterns

Type of crack penetration	Schematic diagram of crack penetration	coherence model	Photographs of representative specimens
tensile penetration		Tensile: wing cracks	
Tension-shear composite penetration		Tension-shear composite: wing cracks, secondary cracks	
shear penetration		Shearability: secondary cracking	

The penetration failure maps of the cracked specimens are grouped according to the crack length L to investigate the influence of the crack geometry parameters on the crack penetration pattern of the specimens. At the same time, use the DFN module in PFC^{2D} to output the crack extension of the specimen, and compare the crack extension simulation results with the indoor test to analyse the influence of the crack geometry parameters on the crack penetration failure pattern of the specimen, as shown in Figs. 13 to 16.

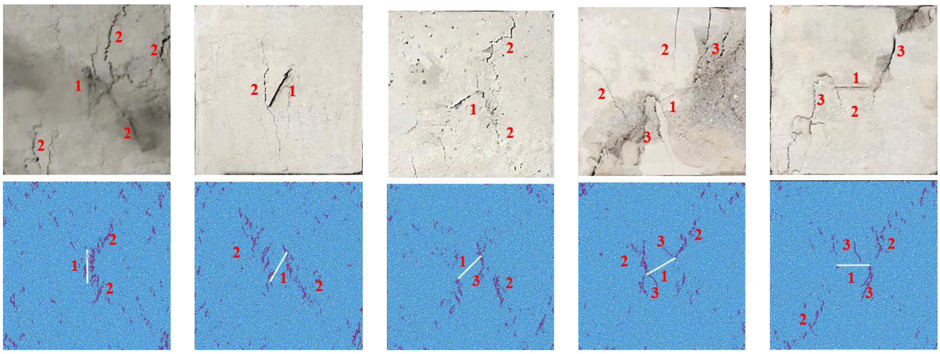

(a) (b) (c) (d) (e)

Fig. 13. Test and Numerical simulation of crack propagation in L = 20 mm fractured samples: (a) $\alpha = 0°$, (b) $\alpha = 30°$, (c) $\alpha = 45°$, (d) $\alpha = 60°$, (e) $\alpha = 90°$

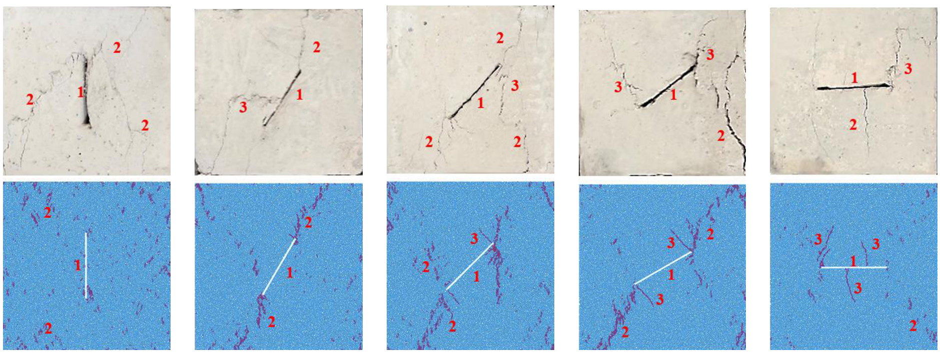

(a) (b) (c) (d) (e)

Fig. 14. Test and Numerical simulation of crack propagation in L = 40 mm fractured samples: (a) $\alpha = 0°$, (b) $\alpha = 30°$, (c) $\alpha = 45°$, (d) $\alpha = 60°$, (e) $\alpha = 90°$

By observing Figs. 13–16, comparing and analysing the crack extension pattern of different crack angles under the same crack length. It can be found that: the crack extension pattern of the specimen under biaxial loading has no obvious pattern to follow by the influence of crack length, and it is more obviously affected by the influence of crack inclination angle. At a crack inclination of 0°, the stress concentration phenomenon at the tip of the prefabricated crack is not obvious enough, and the presence of cracks is mainly dominated by tensile cracks. The stress concentration at the tip of the prefabricated crack was already obvious at a crack inclination of 30°. The crack existence form is still dominated by tensile cracks, and the penetration pattern of the specimen is still dominated by tensile penetration. When the crack inclination angle is 45°, shear cracks represented by quasi-coplanar secondary cracks and tilted secondary cracks gradually appear, and the specimen penetration pattern changes from tensile penetration dominance to the simultaneous existence of tensile penetration and tensile-shear penetration. When the crack inclination angle is 60°, the prefabricated crack end produces multiple inclined secondary cracks, and there is a more obvious “shearing” phenomenon at the end, which is caused by the stress concentration at the end due to the strong axial pressure. Cracks sprouted from the crack end of the specimen, resulting in a more obvious ‘V’ type bifurcation consisting of anti-wing cracks and inclined secondary cracks, and thus expanding to the corner end and the middle of the specimen. When the crack inclination angle is 90°, the specimens with different crack lengths show a convergent and uniform damage pattern, dominated by inclined secondary cracks, and the penetration pattern of the specimens is also uniformly shear penetration.The crack extension law is basically consistent with the law summarised by Wu, X [14], when the inclination angle is small, the tensile crack is dominated, the larger the inclination angle of the prefabricated crack, the larger the initial crack angle, the easier it is to produce stress concentration sprouting secondary cracks. The crack generation location and distribution trend is consistent with the study of Sun, X [7].

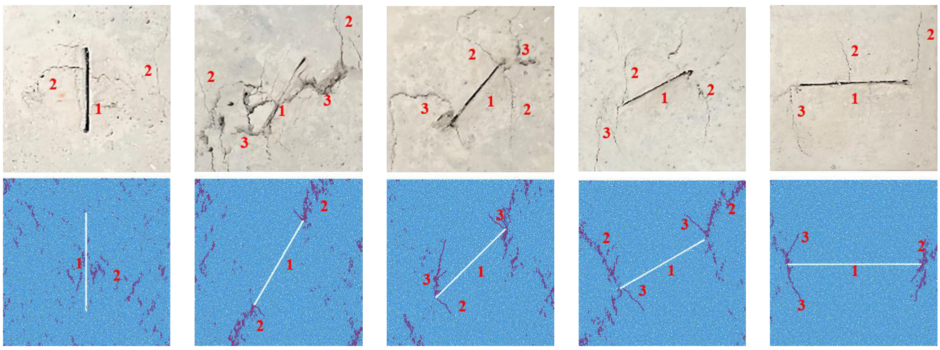

(a) (b) (c) (d) (e)

Fig. 15. Test and Numerical simulation of crack propagation in L = 60 mm fractured samples: (a) $\alpha = 0°$, (b) $\alpha = 30°$, (c) $\alpha = 45°$, (d) $\alpha = 60°$, (e) $\alpha = 90°$

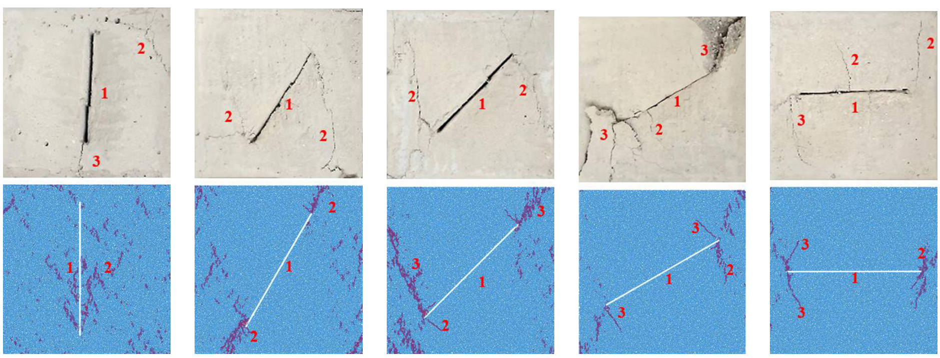

(a) (b) (c) (d) (e)

Fig. 16. Test and Numerical simulation of crack propagation in L = 80 mm fractured samples: (a) $\alpha = 0°$, (b) $\alpha = 30°$, (c) $\alpha = 45°$, (d) $\alpha = 60°$, (e) $\alpha = 90°$. Note: The above diagrams are labelled 1 for prefabricated cracks; 2 for wing cracks (tension cracks); and 3 for secondary cracks (shear cracks)

In summary, tensile penetration mainly occurs at crack inclination angles from 0° to 45°, tensile-shear composite penetration from 45° to 60°, it is worth noting that, although the change in inclination angle from 45° to 60° is small, the stress on the crack end gradually changes from tension to shear, and the stress concentration becomes more obvious, resulting in a reduction in the number of tensile cracks, an increase in the number of secondary cracks and more unstable, which aggravates the phenomenon of crack expansion and 'shear' fall, and shear penetration at 90°. However, the appearance of cracks is not absolute, and this conclusion is more stable for the numerical simulation results, while for the crack evolution of the specimens in the indoor tests, this conclusion is not absolute, and cracks of different natures may appear in each specimen. In general, the crack extension patterns from numerical simulations of rock models with different fracture types under biaxial cyclic loading conditions are more consistent with those obtained from indoor tests.

6. Conclusions

1. For both conventional and cyclic loading and unloading, at a certain lateral pressure, the crack geometry has little effect on the overall shape of the stress-strain curve of the specimen, but does have an effect on the peak stress. An increase in lateral pressure leads to a change in the overall shape of the curve and increases the peak strength of the specimen under external loading. Cyclic loading and unloading at the same lateral pressure have a weakening effect on the rock-like specimens with crack, resulting in peak stresses that are slightly smaller than those of the conventionally loaded specimens under the same conditions.
2. The peak stress of rock-like specimens with crack and the crack inclination angle show a more obvious "V" type relationship, in the same crack length, the crack inclination angle of 45°, the lowest strength of the specimen, from 45° narrowing to 0° or from 45° to 90°, will make the specimen strength increase. The peak stress of the rock specimens of crack type at the same inclination angle will be deteriorated continuously due to the expansion of the crack length and deteriorated due to the convergence of the crack inclination angle to 45°, and these two kinds of deterioration will have a joint effect.
3. The crack penetration mode of rock-like specimens with crack under loading is mainly divided into tensile penetration, shear penetration and tensile-shear composite penetration. Tensile penetration mainly occurs when the crack inclination angle is 0°–30°, tensile-shear composite penetration mainly occurs when the crack inclination angle is 45°–60°, and shear penetration mainly occurs when the crack inclination angle is 90°. Whether the development of the wing crack is restricted or not determines whether the specimen is damaged by the initial crack extension or by the fracture of the specimen itself, which in turn determines the macroscopic damage mode of the specimen. This paper investigates the deformation and damage mechanisms and strength characteristics of fractured rock bodies by conducting biaxial conventional loading tests and biaxial cyclic loading and unloading tests on fractured sandstone specimens and combining them with numerical simulations, which is of great significance in predicting the engineering stability of rock

bodies and in maintaining the construction and operation of underground engineering. Although this study is relevant, there are still some limitations: 1) the influence of factors such as the upper and lower limits of cyclic loading on the tests was not explored in depth; 2) deep rock bodies are generally in a pressurised water environment, and the study of the mechanical properties and damage mechanism of fractured rock bodies under water pressure is also of great practical significance.

References

[1] E. Sahouryeh, A.V. Dyskin, and L.N. Germanovich, "Crack growth under biaxial compression", *Engineering Fracture Mechanics*, vol. 69, no. 18, pp. 2187–2198, 2002, doi: 10.1016/S0013-7944(02)00015-2.

[2] S.Q. Yang and H.W. Jing, "Strength failure and crack coalescence behavior of brittle sandstone samples containing a single fissure under uniaxial compression", *International Journal of Fracture*, vol. 168, no. 2, pp. 227–250, 2011, doi: 10.1007/s10704-010-9576-4.

[3] J. Liu, H. Zhang, H. Bian, W. Wen, and L. Zeng, "Uniaxial mechanical properties and failure characteristics of fractured silty mudstone", *KSCE Journal of Civil Engineering*, vol. 28, no. 1, pp. 139–154, 2024, doi: 10.1007/s12205-023-0200-3.

[4] J. Zeng, Q. Wang, Q. Shen, Q. Zeng, and Z. Pang, "Mechanical characteristics and fracture mechanisms of fissured rock mass samples with various opening sizes", *AIP Advances*, vol. 13, no. 8, art. no. 085104, 2023, doi: 10.1063/5.0148576.

[5] Z. Berisavljević, D. Berisavljević, D. Rakić, G. Hadži-Niković, and Z. Radić, "Strength of composite flysch samples under uniaxial compression", *Bulletin of Engineering Geology and the Environment*, vol. 77, no. 2, pp. 791–802, 2018, doi: 10.1007/s10064-017-1009-4.

[6] Q. Meng, M. Zhang, L. Han, H. Pu, and H. Li, "Effects of size and strain rate on the mechanical behaviors of rock specimens under uniaxial compression", *Arabian Journal of Geosciences*, vol. 9, no. 8, art. no. 527, 2016, doi: 10.1007/s12517-016-2559-7.

[7] X. Sun, W. Li, C. Zhang, G. Zhang, and Z. Xia, "Mechanical behaviors and fracture characteristics of sandstone combinations with different pre-crack angles", *KSCE Journal of Civil Engineering*, vol. 27, no. 12, pp. 5388–5400, 2023, doi: 10.1007/s12205-023-1941-8.

[8] Y.L. Zhao, W. Wan, W.J. Wang, M. Wang, and Q.Y. Peng, "Fracture experiments on ordered multi-crack body in rock-like materials under uniaxial compression and numerical simulation of wing cracks", *Chinese Journal of Geotechnical Engineering*, vol. 35, no. 11, pp. 2097–2109, 2013.

[9] X.P. Zhou, H. Cheng, and Y.F. Feng, "An experimental study of crack coalescence behaviour in rock-like materials containing multiple flaws under uniaxial compression", *Rock Mechanics and Rock Engineering*, vol. 47, no. 6, pp. 1961–1986, 2014, doi: 10.1007/s00603-013-0511-7.

[10] J.Z. Tang, S.Q. Yang, W.L. Tian, and Y. Tao, "Effect of confining pressure on mechanics and deformation behavior of sandstone containing a single inclined joint", *European Journal of Environmental and Civil Engineering*, vol. 26, no. 3, pp. 1022–1045, 2022, doi: 10.1080/19648189.2019.1694076.

[11] J.Z. Tang, S.Q. Yang, D. Elsworth, and Y. Tao, "Three-dimensional numerical modeling of grain-scale mechanical behavior of sandstone containing an inclined rough joint", *Rock Mechanics and Rock Engineering*, vol. 54, no. 2, pp. 905–919, 2021, doi: 10.1007/s00603-020-02281-2.

[12] Y. Jiang, H. Luan, Y. Wang, G. Wang, and P. Wang, "Study on macro-meso failure mechanism of pre-fractured rock specimens under uniaxial compression", *Geotechnical and Geological Engineering*, vol. 36, pp. 3211–3222, 2018, doi: 10.1007/s10706-018-0531-x.

[13] A. Bobet and H.H. Einstein, "Fracture coalescence in rock-type materials under uniaxial and biaxial compression", *International Journal of Rock Mechanics and Mining Sciences*, vol. 35, no. 7, pp. 863–888, 1998, doi: 10.1016/S0148-9062(98)00005-9.

[14] X. Wu, "Crack initiation and failure mechanism of granite with single crack", *Geotechnical and Geological Engineering*, vol. 38, no. 1, pp. 651–661, 2020, doi: 10.1007/s10706-019-01053-2.

[15] X.P. Zhang and L.N.Y. Wong, "Cracking processes in rock-like material containing a single flaw under uniaxial compression: a numerical study based on parallel bonded-particle model approach", *Rock Mechanics and Rock Engineering*, vol. 45, no. 5, pp. 711–737, 2012, doi: 10.1007/s00603-011-0176-z.

[16] H. Haeri, V. Sarfarazi, A. Hedayat, and A. Tabaroei, "Effect of tensile strength of rock on tensile fracture toughness using experimental test and PFC2D simulation", *Journal of Mining Science*, vol. 52, no. 4, pp. 647–661, 2016, doi: 10.1134/S1062739116041046.

[17] H. Haeri, V. Sarfarazi, M. Yazdani, A.B. Shemirani, and A. Hedayat, "Experimental and numerical investigation of the center-cracked horseshoe disk method for determining the mode I fracture toughness of rock-like material", *Rock Mechanics and Rock Engineering*, vol. 51, no. 1, pp. 173–185, 2018, doi: 10.1007/s00603-017-1310-3.

[18] L. Xiong, H. Chen, Z. Xu, and D. Hu, "Numerical simulation study on mechanical properties of rock like specimen with cracks under the coupling of loading and unloading and osmotic pressure", *Archives of Civil Engineering*, vol. 70, no. 3, pp. 297–312, 2024, doi: 10.24425/ace.2024.150984.

[19] M. Bahaaddini, G. Sharrock, and B.K. Hebblewhite, "Numerical investigation of the effect of joint geometrical parameters on the mechanical properties of a non-persistent jointed rock mass under uniaxial compression", *Computers and Geotechnics*, vol. 49, pp. 206–225, 2013, doi: 10.1016/j.compgeo.2012.10.012.

[20] J. Bi, X.P. Zhou, and Q.H. Qian, "The 3D numerical simulation for the propagation process of multiple pre-existing flaws in rock-like materials subjected to biaxial compressive loads", *Rock Mechanics and Rock Engineering*, vol. 49, no. 5, pp. 1611–1627, 2016, doi: 10.1007/s00603-015-0867-y.

[21] R. Peng and T. Zhuang, "Study on meso-fracture behavior and fractal characteristics of sandstone with different particle sizes under compression-shear test conditions", *KSCE Journal of Civil Engineering*, vol. 27, no. 7, pp. 3133–3147, 2023, doi: 10.1007/s12205-023-2251-x.

[22] L. Liu, H. Li, D. Wu, J. Zhou, S. Fu, and X. Li, "Mechanical characteristics and failure process of fractured rocks with a single pre-existing flaw: DEM simulation based on discrete fracture network", in *55th US Rock Mechanics/Geomechanics Symposium*, ARMA, 2021, art. no. ARMA-2021-1130.

[23] G. Sivakumar and V.B. Maji, "Study on crack growth behaviour in rocks having pre-existing narrow flaws under biaxial compression", *Geotechnical and Geological Engineering*, vol. 41, no. 1, pp. 153–188, 2023, doi: 10.1007/s10706-022-02272-w.

Received: 2024-12-30, Revised: 2025-04-21